Optimal Design and Control of a Decoupled Multifrequency Multiphase Wireless Switched Reluctance Motor Drive System

Jun Cai, *Senior Member, IEEE*, Bin Li, Adrian David Cheok, *Senior Member, IEEE*, Ying Yan, *Member, IEEE*, and Xin Zhang, *Senior Member, IEEE*

***Abstract*—In this article, the optimal design and control of a decoupled multifrequency multiphase wireless switched reluctance motor (SRM) drive system are presented. In the proposed system, the single or dual-phase windings of the SRM can be selectively excited by varying the operating frequencies of the inverter. The overall design procedure of the system topology is presented to achieve the stable operation of the SRM and improve the transmission efficiency. In detail, cross-interference can be suppressed with the secondary trap filters, while the primary compensation network is designed to achieve power equalization of the targeted phases and the soft switching of the inverter. Additionally, a dual-state drive method is used to control a single inverter. This method includes a single-frequency half-bridge-driven state and a dual-frequency full-bridge-driven state, which are respectively applied to the single-phase excitation mode and the dual-phase excitation mode, thereby reducing voltage ripples during mode switch. Finally, the hybrid excitation strategy, which is integrated with the dual-state drive method, is utilized to switch the excitation modes, thus achieving the overlapped conduction of the windings and commutation control of the SRM. The feasibility of the proposed system is verified via experiments.**

***Index Terms*—Compensation network design, cross-interference suppression, hybrid excitation strategy, multi-frequency multiphase wireless power transfer, wireless switched reluctance motor (SRM).**

Manuscript received 14 December 2023; revised 15 February 2024 and 6 April 2024; accepted 25 April 2024. Date of publication 13 May 2024; date of current version 20 June 2024. This work was supported in part by the National Natural Science Foundation of China under Grant 52077105, in part by the Natural Science Foundation of Jiangsu Province China under Grant BK20211285, in part by Excellent Research and Innovation Teams in Universities in Anhui Province under Grant 2023AH010021, and in part by the Open Foundation of Key Laboratory of Technology and Equipment of Tianjin Urban Air Transportation System under Grant TJKL-UAM-202301. Recommended for publication by Associate Editor D. Dujic. *(Corresponding author: Jun Cai.)*

Jun Cai is with the C-MEIC, CICAEET, and the School of Automation, Nanjing University of Information Science and Technology, Nanjing 210044, China, and also with Anhui Jianzhu University, Hefei 230009, China (e-mail: j.cai@nuist.edu.cn).

Bin Li, Adrian David Cheok, and Ying Yan are with the C-MEIC, CICAEET, and the School of Automation, Nanjing University of Information Science and Technology, Nanjing 210044, China (e-mail: binli@nuist.edu.cn; adrian@imagineeringinstitute.org; ying.yan@nuist.edu.cn).

Xin Zhang is with the College of Electrical Engineering, Zhejiang University, Hangzhou 310027, China (e-mail: zhangxin_ieee@zju.edu.cn).

Color versions of one or more figures in this article are available at https://doi.org/10.1109/TPEL.2024.3399737.

Digital Object Identifier 10.1109/TPEL.2024.3399737

I. Introduction

WIRELESS power transfer (WPT) is an epoch-making technique with the advantages of high flexibility, good convenience, and electrical isolation, which has been widely used in electric vehicles [1], industrial robots [2], and implantable medical devices [3]. Compared with the single-receiver WPT systems, it is more attractive for multireceiver/multiphase WPT (MR/MP-WPT) systems to power multiple loads selectively or simultaneously with the single transmitter. The receivers of MR/MP-WPT systems can be designed with single frequency or multiple frequencies. The conventional single-frequency MR/MP-WPT system requires secondary dc–dc converters or active compensators to control the power flows independently [4], [5]. Nevertheless, the active parts of the receivers involve complex control strategies and result in additional loss. Hence, the multifrequency MR/MP-WPT system is proposed in [6] and [7]. In this system, power channels of multiple frequencies can be established by tuning the operating frequencies to the resonant frequencies, and auxiliary converters are removed in the receiving side.

Recently, more and more research has integrated MR/MP-WPT into motor drives, such as brushed dc motors [8], variable-reluctance stepping motor [9], and switched reluctance motor (SRM) [10], [11]. Wireless motor systems utilize magnetically coupled resonant converters, which avoid the use of the power cables between sources and loads [8], [9], [10], [11]. More significantly, the systems provide the possibility to eliminate the switches and controllers on the receiving side. Brushed dc motors or the windings of multiphase motors are sequentially connected to the receivers of the multiphase WPT system. In [8] and [9], multiple half-bridge (HB) inverters are controlled to energize the transmitting coils and power distribution among motors or windings is enabled through a shared power channel. To reduce the number of switches of the transmitter, Jiang et al. [10] and [11] combined the multifrequency selective WPT systems with SRM. In the wireless SRM system, the transmitter's operating frequency is selected to be one of the resonant frequencies of the receivers and windings are excited in a time-division way.

Although numerous attempts have been made to fulfill the wireless SRM systems, there are still some problems that need to be addressed. The cross interference among receivers is one of the problems that can lead to the excitation of nontargeted phases and decrease in efficiency. In [9], the coils on one side are on

the same plane and far apart to reduce the undesirable coupling. However, this results in a large system volume. Bipolar coils or overlapped coils are employed to decouple the transmitters or the receivers [12], [13]. However, the decoupled coils are difficult to design when there are more than three receivers. Although the multifrequency systems proposed in [10] and [11] can be free of the cross-interference, the high load quality factor is needed to reduce the interference from the nontargeted frequency, which brings an increment of voltage stress of receiving coils and capacitors. In [14], the self-resonant frequencies of different load coils are set to different bifurcated frequencies to minimize the cross interference. However, external transmitting coil position control setup is involved to regulate the output power. In [15], three types of compensation circuits are introduced into receivers of the multifrequency system to reduce the cross interference. However, the harmonics of nontargeted frequency, which can also interfere with the targeted load power, are not considered in the design. By adopting the resonant filters in wireless SRM, the interference from odd harmonics of nontargeted channels can be well suppressed [16]. However, the SRM performance is limited due to the lack of overlapping regions in the winding currents.

Another problem is the phase overlap excitation of wireless SRMs in [10], [11], [12], and [16] cannot be achieved, resulting in the restricted torque output and large torque ripple [13]. To energize multiple phases simultaneously, several topologies have been proposed for the multifrequency MR/MP-WPT systems [17], [18], [19], [20], [21]. In [17], the transmitter consists of multiple full-bridge (FB) inverters operating at multiple switching frequencies, and the output of each receiver can be regulated by controlling the duty cycle of the corresponding inverter. However, the system structure is complex. In [18], one diode is connected in series to each inverter leg, and the harmonics of square waveforms generated by the single inverter are utilized to charge the receivers. However, the power of each load/phase cannot be regulated individually. The multilevel inverter is employed to realize multifrequency superposition, and the transmitted energy in each power channel can be controlled separately [19]. However, additional switching loss and cost are added due to the increase in power switches. In [20] and [21], based on sinusoidal pulse width modulation, multifrequency modulation waves are superimposed to drive the single FB inverter. Then, the wireless power supply for loads can be independently controlled by changing the amplitude of modulation waves. However, the inverter operates at the carrier frequency, which is much higher than the frequency of modulation waves. Hence, efficiency is reduced due to the increased switching loss.

This article proposes a decoupled multifrequency multiphase wireless SRM with a hybrid excitation strategy. The main contributions of this article are summarized as follows.

1) A dual-state drive method is proposed to control the single inverter, which includes single-frequency HB-driven state and dual-frequency FB-driven state. Meanwhile, the frequency of each output voltage component of the inverter can be regulated to select single or dual target phases among the receivers.
2) With the elaborate design of the *LCC* compensation on the transmitting side, power equalization for multiple phases is achieved and soft switching of the inverter in the single-phase excitation mode (SPEM) is realized to enhance the efficiency.

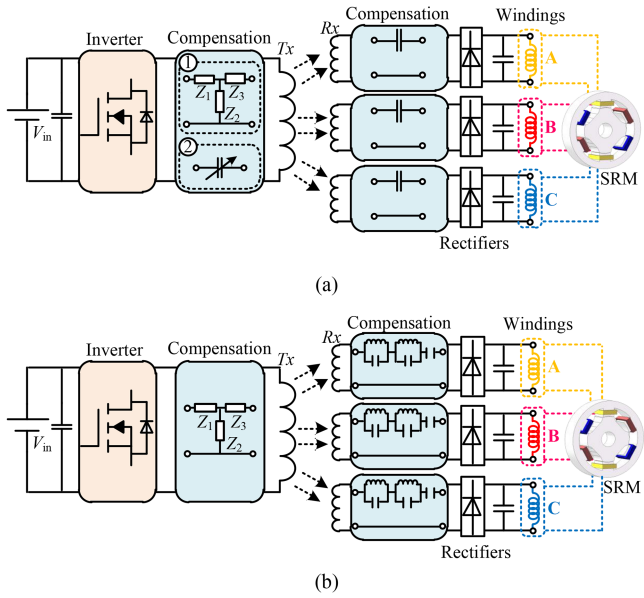

Fig. 1. Comparison of the multifrequency multiphase wireless SRM system topologies. (a) Conventional topology with series compensation on the receiving side [10], [11]. (b) Proposed topology with TFs on the receiving side.

3) Trap filters (TFs) are designed for the receivers to reduce cross interference from the nontargeted resonant frequencies and their high-order harmonics.
4) Based on the commutation control sequence, the hybrid excitation strategy is utilized to shift the SPEM and dual-phase excitation mode (DPEM) according to the rotor position, thus achieving the phase-overlapped excitation of SRM.

The rest of this article is organized as follows. In Section II, the topology and operation principles of the proposed system are presented. Then, the system circuit design and control methods are discussed in Sections III and IV, respectively. Moreover, the experimental prototype is constructed to verify the feasibility of the proposed system in Section V. Finally, the conclusion is made in Section VI.

II. Proposed Decoupled Multifrequency Multiphase Wireless SRM System

A. Comparison of the Multifrequency Multiphase Wireless SRM System Topologies

The SRM has a simple structure and does not include a permanent magnet [22]. The phase windings of the SRM operate independently, offering high reliability and strong fault tolerance [23]. Moreover, the wireless SRM does not require switches and controllers on the motor side, making it well-suited for harsh environments.

Topologies of wireless SRM systems are shown in Fig. 1, where the transmitting coil and the receiving coils are represented as *Tx* and *Rx*, respectively. As shown in Fig. 1(a), the high-order compensation which is composed of impedances Z_1, Z_2, and Z_3, or switched capacitors are utilized to compensate the reactive power of the transmitting coil and series compensations are adopted in the receiving side [10], [11]. The phase windings can be energized sequentially by changing the operating

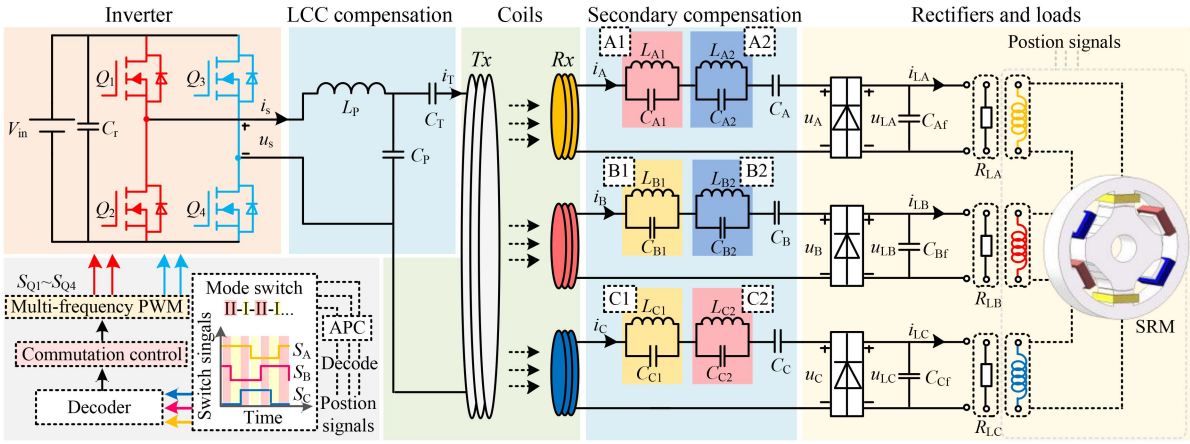

Fig. 2. Configuration of the proposed decoupled multifrequency multiphase wireless SRM system.

frequencies. To reduce the torque ripple, power equalization of multiple phases is required. Hence, with the symmetrical coupling condition, the resonant frequencies of the receivers are designed to be close enough. When the equivalent load of the motor decreases, the cross interference of power channels occurs due to the reduced load quality factor [15]. In order to address the problem, the decoupled multifrequency multiphase WPT topology is proposed for the wireless SRM system, in which the TFs are designed for the receivers to reduce the cross-interference, as shown in Fig. 1(b).

B. Overall Configuration of the Proposed Multifrequency Multiphase Wireless SRM Drive System

It should be noted that the equivalent load of the inductive winding, which is viewed from the ac side of the rectifier, is purely resistive [24] and can be considered as a constant resistance at a steady state of speed and torque [10], [11]. Hence, in this article, both the resistive loads and SRM are utilized to demonstrate the design and control methods of the proposed decoupled multifrequency wireless SRM system. As shown in Fig. 2, the proposed system includes a single transmitter and three receivers. The transmitter contains a dc voltage source ($V_{\rm in}$), MOSFETs (Q_1–Q_4), *LCC* compensation network, and the transmitting coil. The *LCC* compensation is formed by the series inductor ($L_{\rm P}$), the parallel and series capacitors ($C_{\rm P}$ and $C_{\rm T}$), which makes the transmitter resonant at frequency of $f_{\rm p}$. Each receiver contains a receiving coil ($L_{\rm m}$, m = A, B, C), a TF, a series capacitor ($C_{\rm m}$), a rectifier, and a load ($R_{\rm Lm}$), which can be a resistance or a winding. The TF of each receiver consists of dual parallel resonant units, where $L_{\rm m1}/L_{\rm m2}$ and $C_{\rm m1}/C_{\rm m2}$ are the parallel inductors and the corresponding capacitors, respectively. $u_{\rm S}$ and $i_{\rm S}$ are the inverter output voltage and current, respectively; $i_{\rm T}$ and $i_{\rm m}$ are the current of the transmitting coil and receiving coils, respectively; $u_{\rm m}$ is the voltage in the ac side of rectifiers; $u_{\rm Lm}$ and $i_{\rm Lm}$ are the load voltage and current, respectively.

The receivers of the proposed wireless SRM are designed with different resonant frequencies, namely, $f_{\rm m}$ (m = A, B, C). Then, by tuning the operating frequencies of the primary inverter to the receivers' resonant frequencies, the power channels can be built and then the specific phase windings are excited. There are two operating modes in this system: 1) Mode I, SPEM: the energy is transmitted to only one of the three phases at the same time; 2) Mode II, DPEM: the transmitter powers two of the three phases at the same time.

A dual-state drive method is proposed to control the inverter, which includes the single-frequency HB-driven state and the dual-frequency FB-driven state. The bridge leg I operates at frequency $f_{\rm o1}$, while bridge leg II operates at frequency of $f_{\rm o2}$, and $f_{\rm o1} \neq f_{\rm o2}$.

1) Single-frequency HB-driven state is utilized in SPEM. The power switches Q_1 and Q_2 of the bridge leg I are controlled by PWM signals with frequency of $f_{\rm o1}$. Q_3 is cutoff and Q_4 maintains conduction, which means bridge leg II works at the frequency of $f_{\rm o2} = 0$ Hz and the FB inverter is controlled as a single-frequency-driven HB inverter. As a result, only the phase with the resonant frequency of $f_{\rm o1}$ is excited.
2) Dual-frequency FB-driven state is adopted in DPEM, where $f_{\rm oi}$ (i = 1, 2) is taken as the resonant frequencies of the receivers. As a result, the two phases with resonant frequencies of $f_{\rm o1}$ and $f_{\rm o2}$ are excited.

Additionally, the hybrid excitation strategy is utilized to shift operating modes to achieve the phase-overlapped excitation of SRM. With the motion direction and rotor position, angular position control (APC) is used to generate the switch signals. Then, the target phase(s) and the operating frequencies are selected with the commutation control. Finally, control signals of the inverter are generated and the target(s) can be energized.

C. Modeling of the Proposed System

In DPEM, the fundamental harmonics of the inverter output ac voltages at frequencies of $f_{\rm o1}$ and $f_{\rm o2}$ are regarded as phasors $U_{\rm S}^{(1)}$ and $U_{\rm S}^{(2)}$, respectively. In SPEM, the fundamental frequency of the ac source equals to $f_{\rm o1}$ and $f_{\rm o2} = 0$ Hz, which means only $U_{\rm S}^{(1)}$ is validated and $U_{\rm S}^{(2)} = 0$. As a result, SPEM can be considered as a special case of the DPEM, and only the model of the system in DPEM is elaborated as follows.

The equivalent circuit of the proposed system is shown in Fig. 3, where $L_{\rm T}$ and $R_{\rm T}$ are the inductance and resistance of the transmitting coil; $M_{\rm Tm}$ is the mutual inductance between the transmitter and the receivers; $M_{\rm mg}$ (g = A, B, C, $m \neq g$) is the mutual inductance between the receivers; $L_{\rm m}$ and $R_{\rm m}$ represent the inductance and resistance of the receiving coil; $R_{\rm Leqm}$ is the

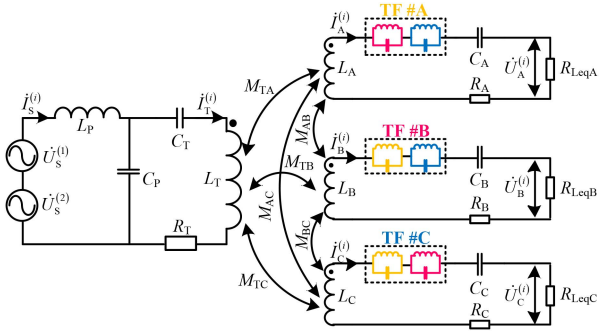

Fig. 3. Equivalent circuit of the decoupled multifrequency multiphase wireless SRM system.

equivalent load converted to the ac side of the rectifier, where $R_{\mathrm{Leqm}} = (8/\pi^2)\times R_{\mathrm{Lm}}$. To compensate the inductances of coils, resonant components on both sides can be calculated as

$$j\omega_{\mathrm{p}}L_{\mathrm{P}} = -\frac{1}{j\omega_{\mathrm{p}}C_{\mathrm{P}}} = j\omega_{\mathrm{p}}L_{\mathrm{T}} + \frac{1}{j\omega_{\mathrm{p}}C_{\mathrm{T}}} \tag{1}$$

$$j\omega_{\mathrm{m}}L_{\mathrm{m}} + \frac{1}{j\omega_{\mathrm{m}}C_{\mathrm{m}}} + \frac{j\omega_{\mathrm{m}}L_{\mathrm{m1}}}{1-\omega_{\mathrm{m}}^2 L_{\mathrm{m1}}C_{\mathrm{m1}}} + \frac{j\omega_{\mathrm{m}}L_{\mathrm{m2}}}{1-\omega_{\mathrm{m}}^2 L_{\mathrm{m2}}C_{\mathrm{m2}}} = 0 \tag{2}$$

where $\omega_{\mathrm{p}} = 2\pi f_{\mathrm{p}}$ and $\omega_{\mathrm{m}} = 2\pi f_{\mathrm{m}}$. The parallel resonant units of the TFs can be tuned by the equations as follows:

$$\begin{cases} -\omega_{\mathrm{B}}^2 L_{\mathrm{A1}}C_{\mathrm{A1}} + 1 = 0 \\ -\omega_{\mathrm{C}}^2 L_{\mathrm{A2}}C_{\mathrm{A2}} + 1 = 0 \end{cases} \tag{3}$$

$$\begin{cases} -\omega_{\mathrm{A}}^2 L_{\mathrm{B1}}C_{\mathrm{B1}} + 1 = 0 \\ -\omega_{\mathrm{C}}^2 L_{\mathrm{B2}}C_{\mathrm{B2}} + 1 = 0 \end{cases} \tag{4}$$

$$\begin{cases} -\omega_{\mathrm{A}}^2 L_{\mathrm{C1}}C_{\mathrm{C1}} + 1 = 0 \\ -\omega_{\mathrm{B}}^2 L_{\mathrm{C2}}C_{\mathrm{C2}} + 1 = 0 \end{cases} \tag{5}$$

According to Kirchhoff's voltage law, the circuit model at the frequency f_{oi} can be expressed as (6) is shown at the bottom of this page, where $\omega_{\mathrm{oi}} = 2\pi f_{\mathrm{oi}}$ and the superscript i indicates the operating frequency. $Z_{\mathrm{m}}^{(i)}$ is the impedance of the receiver m, which can be expressed as

$$Z_{\mathrm{m}}^{(i)} = j\omega_{\mathrm{oi}}L_{\mathrm{m}} + \frac{1}{j\omega_{\mathrm{oi}}C_{\mathrm{m}}} + \frac{j\omega_{\mathrm{oi}}L_{\mathrm{m1}}}{1-\omega_{\mathrm{oi}}^{2L_{\mathrm{m1}}C_{\mathrm{m1}}}} + \frac{j\omega_{\mathrm{oi}}L_{\mathrm{m2}}}{1-\omega_{\mathrm{oi}}^2 L_{\mathrm{m2}}C_{\mathrm{m2}}} + R_{\mathrm{m}} + R_{\mathrm{Leqm}}. \tag{7}$$

The current phasors $I_{\mathrm{S}}^{(i)}$, $I_{\mathrm{T}}^{(i)}$, and $I_{\mathrm{m}}^{(i)}$ can be derived by solving (6) and $I_{\mathrm{m}}^{(i)}$ can be given by

$$\dot{I}_{\mathrm{m}}^{(i)} = \frac{j\omega_{\mathrm{oi}}M_{\mathrm{Tm}}\dot{I}_{\mathrm{T}}^{(i)}}{Z_{\mathrm{m}}^{(i)}} = \frac{j\omega_{\mathrm{oi}}M_{\mathrm{Tm}}\dot{U}_{\mathrm{S}}^{(i)}\left(1-\frac{j\omega_{\mathrm{oi}}L_{\mathrm{P}}}{Z_{\mathrm{S}}^{(i)}}\right)}{Z_{\mathrm{m}}^{(i)}\left(j\omega_{\mathrm{oi}}L_{\mathrm{T}} + \frac{1}{j\omega_{\mathrm{oi}}C_{\mathrm{T}}} + R_{\mathrm{T}} + Z_{\mathrm{r}}^{(i)}\right)} \tag{8}$$

where $Z_{\mathrm{r}}^{(i)}$ is the total reflected impedance, and the input impedance of the system $Z_{\mathrm{S}}^{(i)}$ can be calculated as

$$Z_{\mathrm{S}}^{(i)} = j\omega_{\mathrm{oi}}L_{\mathrm{P}} + \frac{1}{j\omega_{\mathrm{oi}}C_{\mathrm{P}}} // \left(j\omega_{\mathrm{oi}}L_{\mathrm{T}} + \frac{1}{j\omega_{\mathrm{oi}}C_{\mathrm{T}}} + R_{\mathrm{T}} + Z_{\mathrm{r}}^{(i)}\right) \tag{9}$$

where $Z_{\mathrm{r}}^{(i)}$ is composed of the reflected impedance of phases A, B, and C, namely, $Z_{\mathrm{rA}}^{(i)}$, $Z_{\mathrm{rB}}^{(i)}$, and $Z_{\mathrm{rC}}^{(i)}$, which can be expressed as (10) is shown at the bottom of the next page. When one of the operating frequencies is tuned to the resonant frequency of phase A, namely $f_{\mathrm{oi}} = f_{\mathrm{A}}$, the imaginary part of Z_{A} is equal to 0. Moreover, according to (4) and (5), the parallel resonant units B1 and C1 produce a high impedance at the frequency f_{A}, and Z_{B} as well as Z_{C} are much larger than Z_{A}, $(\omega_{\mathrm{oi}}M_{\mathrm{Tm}})^2$ and $\omega_{\mathrm{oi}}M_{\mathrm{mg}}$. As a result, the value of $Z_{\mathrm{rA}}^{(i)}$ is much greater than that of $Z_{\mathrm{rB}}^{(i)}$ and $Z_{\mathrm{rC}}^{(i)}$, which means most of the energy at frequency f_{A} flows to R_{LA}. In this case, $Z_{\mathrm{r}}^{(i)}$ can be expressed as

$$\begin{aligned} Z_{\mathrm{r}}^{(i)} &= Z_{\mathrm{rA}}^{(i)} + Z_{\mathrm{rB}}^{(i)} + Z_{\mathrm{rC}}^{(i)} \\ &= \frac{\omega_{\mathrm{oi}}^2 M_{\mathrm{TA}}^2}{Z_{\mathrm{A}}^{(i)}} + \frac{\omega_{\mathrm{oi}}^2 M_{\mathrm{TB}}^2}{Z_{\mathrm{B}}^{(i)}} + \frac{\omega_{\mathrm{oi}}^2 M_{\mathrm{TC}}^2}{Z_{\mathrm{C}}^{(i)}} \approx \frac{\omega_{\mathrm{oi}}^2 M_{\mathrm{TA}}^2}{Z_{\mathrm{A}}^{(i)}} \quad (\omega_{\mathrm{oi}} = \omega_{\mathrm{A}}). \end{aligned} \tag{11}$$

Similarly, when $f_{\mathrm{oi}} = f_{\mathrm{B}}$ and $f_{\mathrm{oi}} = f_{\mathrm{C}}$, the total reflected impedance $Z_{\mathrm{r}}^{(i)}$ equals to $(\omega_{\mathrm{oi}}M_{\mathrm{TB}})^2/Z_{\mathrm{B}}^{(i)}$ and $(\omega_{\mathrm{oi}}M_{\mathrm{TC}})^2/Z_{\mathrm{C}}^{(i)}$, respectively.

Based on the parameters shown in Table I, characteristics of the reflected impedance in frequency domain are depicted in Fig. 4, where R_{Lm} is 5.2 Ω at motor speed of 1500 r/min. The ratio of Z_{rA}, Z_{rB}, and Z_{rC} indicates the power distribution ratio among the receivers [25]. As shown in Fig. 4(a) and (b), it can be seen that, with series compensation on the receiving side, the resonances for phases A, B, and C occur at their targeted resonant frequencies, namely 90, 110, and 130 kHz, respectively. However, there is serious cross-interference among the receivers. For example, when $f_{\mathrm{oi}} = f_{\mathrm{A}} = 90$ kHz, although $|Z_{\mathrm{rA}}|$ in Fig. 4(a) is the largest and most of the power is transmitted to phase A, the values of $|Z_{\mathrm{rB}}|$ and $|Z_{\mathrm{rC}}|$ are not negligible compared with $|Z_{\mathrm{rA}}|$. Hence, phase B and phase C can be excited by the energy at their nontargeted resonant frequency f_{A}, which means the excitation target cannot be selected. Instead, as shown in Fig. 4(c) and (d), $|Z_{\mathrm{rA}}| >> |Z_{\mathrm{rB}}|$ and $|Z_{\mathrm{rA}}| >> |Z_{\mathrm{rC}}|$ at the frequency 90 kHz can be achieved, which indicates that the TFs at receivers B and C

$$\begin{bmatrix} \dot{U}_{\mathrm{S}}^{(i)} \\ 0 \\ 0 \\ 0 \\ 0 \end{bmatrix} = \begin{bmatrix} j\omega_{\mathrm{oi}}L_{\mathrm{P}} & j\omega_{\mathrm{oi}}L_{\mathrm{T}} + \frac{1}{j\omega_{\mathrm{oi}}C_{\mathrm{T}}} + R_{\mathrm{T}} & -j\omega_{\mathrm{oi}}M_{\mathrm{TA}} & -j\omega_{\mathrm{oi}}M_{\mathrm{TB}} & -j\omega_{\mathrm{oi}}M_{\mathrm{TC}} \\ -\frac{1}{j\omega_{\mathrm{oi}}C_{\mathrm{P}}} & \frac{1}{j\omega_{\mathrm{oi}}C_{\mathrm{P}}} + j\omega_{\mathrm{oi}}L_{\mathrm{T}} + \frac{1}{j\omega_{\mathrm{oi}}C_{\mathrm{T}}} + R_{\mathrm{T}} & -j\omega_{\mathrm{oi}}M_{\mathrm{TA}} & -j\omega_{\mathrm{oi}}M_{\mathrm{TB}} & -j\omega_{\mathrm{oi}}M_{\mathrm{TC}} \\ 0 & -j\omega_{\mathrm{oi}}M_{\mathrm{TA}} & Z_{\mathrm{A}}^{(i)} & j\omega_{\mathrm{oi}}M_{\mathrm{AB}} & j\omega_{\mathrm{oi}}M_{\mathrm{AC}} \\ 0 & -j\omega_{\mathrm{oi}}M_{\mathrm{TB}} & j\omega_{\mathrm{oi}}M_{\mathrm{AB}} & Z_{\mathrm{B}}^{(i)} & j\omega_{\mathrm{oi}}M_{\mathrm{BC}} \\ 0 & -j\omega_{\mathrm{oi}}M_{\mathrm{TC}} & j\omega_{\mathrm{oi}}M_{\mathrm{AC}} & j\omega_{\mathrm{oi}}M_{\mathrm{BC}} & Z_{\mathrm{C}}^{(i)} \end{bmatrix} \begin{bmatrix} \dot{I}_{\mathrm{S}}^{(i)} \\ \dot{I}_{\mathrm{T}}^{(i)} \\ \dot{I}_{\mathrm{A}}^{(i)} \\ \dot{I}_{\mathrm{B}}^{(i)} \\ \dot{I}_{\mathrm{C}}^{(i)} \end{bmatrix}. \tag{6}$$

TABLE I
SYSTEM PARAMETERS

Items	Value
Inductance of transmitting coil (L_T)	141.9 μH
Inductance of receiving coils ($L_A/L_B/L_C$)	106.1/105.6/103.5 μH
Mutual inductance ($M_{TA}/M_{TB}/M_{TC}$)	21.9/21.5/21.3 μH
Mutual inductance between the receivers ($M_{AB}/M_{BC}/M_{AC}$)	6.1/4.9/4.6 μH
Series inductor of LCC compensation (L_P)	34.4 μH
Series capacitor of LCC compensation (C_P)	62.5 nF
Parallel capacitor of LCC compensation (C_T)	20.27 nF
Inductors of trap filters (L_{m1}/L_{m2})	22.5/9.9 μH
Series capacitors of receivers ($C_A/C_B/C_C$)	16.2/22.1/39.7 nF
Resistance of transmitting coil (R_T)	0.19 Ω
Resistance of receiving coil ($R_A/R_B/R_C$)	0.14/0.16/0.2 Ω
Maximum winding inductance (L_{max})	5.4 mH
Minimum winding inductance (L_{min})	1.3 mH
Stator pole pitch (β_S)	30°
Internal winding resistance	5 Ω
Resonant frequencies of the receivers (f_m)	90/110/130 kHz

can suppress the energy interference at frequency f_A. Therefore, the interference of the nontargeted resonant frequencies can be reduced with TFs. In addition, the reflected impedances at the harmonics of the nontargeted resonant frequency also need to be limited, and more details can be seen in Section III-B.

For the phase m, $P_m^{(i)}$ which is the output power at operating frequency f_{oi}, and the total output power P_m can be expressed as

$$P_m^{(i)} = \left|I_m^{(i)}\right|^2 R_{Leqm} \tag{12}$$

$$P_m = P_m^{(1)} + P_m^{(2)}. \tag{13}$$

If $f_{o1} = f_m$ and $f_{o2} \neq f_m$, $Z_r^{(1)} \approx Z_{rm}^{(1)}$ and the energy of the inverter output at frequency f_{o1} mainly flows to the phase m. In addition, the value of the reflected impedance of phase m at frequency f_{o2}, namely $Z_{rm}^{(2)}$, is very small due to the TFs. Consequently, the phase m can hardly receive the power with frequency f_{o2} and $P_m^{(2)} << P_m^{(1)}$. By substituting (8) and (12) into (13), P_m can be calculated as

$$P_m \approx P_m^{(1)} = \left|I_m^{(1)}\right|^2 R_{Leqm} = \frac{\alpha R_{Leqm}}{\beta + \gamma(R_{Leqm}+R_m) + \delta(R_{Leqm}+R_m)^2} \quad (\omega_{o1} = \omega_m) \tag{14}$$

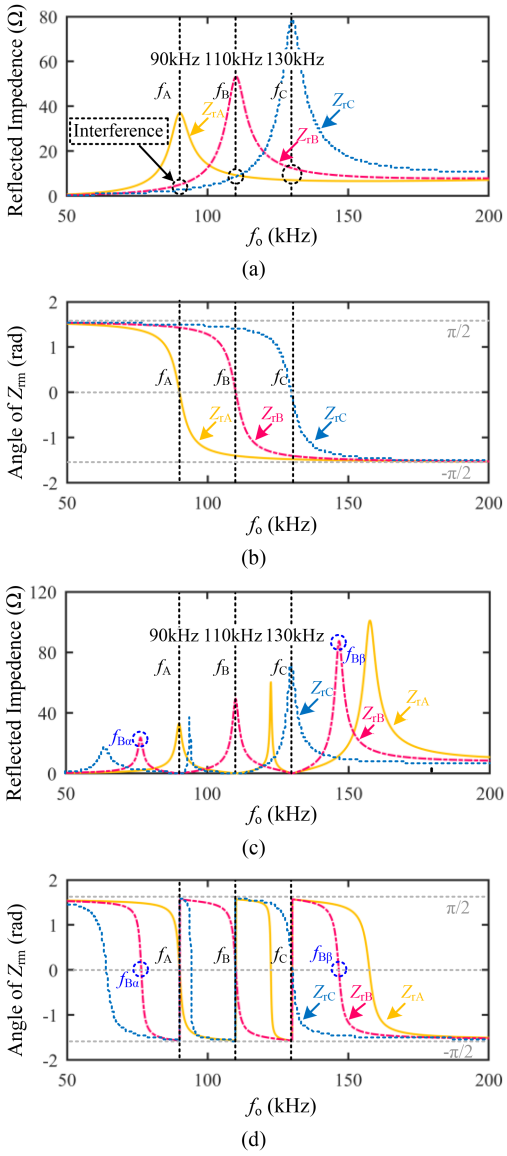

Fig. 4. Characteristics of the reflected impedance. (a) Impedance absolute values with series compensation. (b) Impedance angles with series compensation. (c) Impedance absolute values with TFs. (d) Impedance angles with TFs.

where α, β, γ, and δ can be given by

$$\begin{cases} \alpha = \omega_{o1}^4 \omega_p^4 M_{Tm}^2 U_S^{(i)^2} \\ \beta = \omega_{o1}^6 M_{Tm}^4 \left(\omega_{o1}^2 - \omega_p^2\right)^2 \\ \gamma = 2\omega_{o1}^4 M_{Tm}^2 R_T \left(\omega_{o1}^2 - \omega_p^2\right)^2 \\ \delta = R_T^2 \left(\omega_{o1}^3 - \omega_{o1}\omega_p^2\right)^2 + \left(\omega_{o1}^4 L_P - L_T(\omega_{o1}^2 - \omega_p^2)^2\right)^2 \end{cases}. \tag{15}$$

$$\begin{cases} Z_{rA}^{(i)} = \dfrac{\omega_{oi}^2 M_{TA}^2 Z_B^{(i)} Z_C^{(i)} - j\omega_{oi}^3 M_{TA}(M_{AC}M_{TC}Z_B^{(i)} + M_{AB}M_{TB}Z_C^{(i)}) + \omega_{oi}^4 M_{TA}(M_{TA}M_{BC}^2 - M_{TB}M_{AC}M_{BC} - M_{TC}M_{AB}M_{BC})}{Z_A^{(i)} Z_B^{(i)} Z_C^{(i)} + \omega_{oi}^2 M_{BC}^2 Z_A^{(i)} + \omega_{oi}^2 M_{AC}^2 Z_B^{(i)} + \omega_{oi}^2 M_{AB}^2 Z_C^{(i)} - 2j\omega_{oi}^3 M_{AB}M_{AC}M_{BC}} \\ Z_{rB}^{(i)} = \dfrac{\omega_{oi}^2 M_{TB}^2 Z_A^{(i)} Z_C^{(i)} - j\omega_{oi}^3 M_{TB}(M_{BC}M_{TC}Z_A^{(i)} + M_{AB}M_{TA}Z_C^{(i)}) + \omega_{oi}^4 M_{TB}(M_{TB}M_{AC}^2 - M_{TA}M_{AC}M_{BC} - M_{TC}M_{AB}M_{AC})}{Z_A^{(i)} Z_B^{(i)} Z_C^{(i)} + \omega_{oi}^2 M_{BC}^2 Z_A^{(i)} + \omega_{oi}^2 M_{AC}^2 Z_B^{(i)} + \omega_{oi}^2 M_{AB}^2 Z_C^{(i)} - 2j\omega_{oi}^3 M_{AB}M_{AC}M_{BC}} \\ Z_{rC}^{(i)} = \dfrac{\omega_{oi}^2 M_{TC}^2 Z_A^{(i)} Z_B^{(i)} - j\omega_{oi}^3 M_{TC}(M_{BC}M_{TB}Z_A^{(i)} + M_{AC}M_{TA}Z_B^{(i)}) + \omega_{oi}^4 M_{TC}(M_{TC}M_{AB}^2 - M_{TA}M_{AB}M_{BC} - M_{TB}M_{AB}M_{AC})}{Z_A^{(i)} Z_B^{(i)} Z_C^{(i)} + \omega_{oi}^2 M_{BC}^2 Z_A^{(i)} + \omega_{oi}^2 M_{AC}^2 Z_B^{(i)} + \omega_{oi}^2 M_{AB}^2 Z_C^{(i)} - 2j\omega_{oi}^3 M_{AB}M_{AC}M_{BC}} \end{cases} \tag{10}$$

On the contrary, if $f_{o2}=f_m$ and $f_{o1}\neq f_m$, $P_m \approx P_m^{(2)}$ and the model of P_m can be obtained by replacing ω_{o1} with ω_{o2} in (14) and (15). If $f_{o1}\neq f_m$ and $f_{o2}\neq f_m$, the phase m receives no power due to the small reflected impedance.

The output voltage of phase m can be expressed as

$$U_{Lm}=\sqrt{P_m R_{Lm}}. \tag{16}$$

The angle of the input impedance of the system can be calculated as

$$\varphi^{(i)}=\arctan\left(\frac{\mathrm{Im}\left(Z_S^{(i)}\right)}{\mathrm{Re}\left(Z_S^{(i)}\right)}\right). \tag{17}$$

The input power P_{in} can be given by

$$P_{in}=\sum_{i=1}^{2}P_{in}^{(i)}=\sum_{i=1}^{2}\left|U_S^{(i)}\right|\left|I_S^{(i)}\right|\cos\varphi^{(i)} \tag{18}$$

where $P_{in}^{(i)}$ is the input power at operating frequency f_{oi}.

If $f_{o1}=f_m$ and $f_{o2}=f_g$, the phase m and g are excited, and the system transmission efficiency η can be expressed as

$$\eta=\frac{P_m+P_g}{P_{in}}=\frac{P_m+P_g}{\sum_{i=1}^{2}\left|U_S^{(i)}\right|\left|I_S^{(i)}\right|\cos\varphi^{(i)}}. \tag{19}$$

III. System Design

A. LCC *Compensation Design*

The dc source V_{in} and the required load voltage U_{ref} are set to 96 and 24 V, respectively. In order to obtain a moderate transmission distance and achieve the high-efficient operation, the operating frequencies are set to 90, 110, and 130 kHz. The overall parameters are shown in Table I.

From (14) and (15) in Section II-C, it can be seen that the output power P_m can be adjusted by regulating f_p and L_p. With $L_p = 34.4\ \mu$H, phases A, B, and C are selected as the excitation target in SPEM, respectively, and the corresponding output voltages are denoted as U_{LA}, U_{LB} and U_{LC}, as shown in Fig. 5(a). U_{Lmin} is the minimum value of three-phase voltages and the black dashed line in Fig. 5(a) shows the relationship between U_{Lmin} and f_p. The valid range of U_{Lmin}, which satisfies the required output voltage U_{ref}, can be located in Fig. 5(b), and the corresponding f_p and L_p can be found. Then, since the equivalent resistances of motor windings are assumed to be symmetrical, the cross points of U_{LA}, U_{LB}, and U_{LC} are selected to achieve power equalization among the receivers, and the corresponding f_p are 109 and 133 kHz, as shown in Fig. 5(a).

Moreover, zero voltage switching (ZVS) of the inverter can be realized to improve the efficiency by designing the input impedance angle φ to be inductive in SPEM. However, it is difficult to achieve ZVS when the components of the inverter output contain operating frequencies with noninteger multiples, and the ZVS in DPEM will be studied in the future. As shown in Fig. 5(c), the input impedance Z_S at each operating frequency is inductive when $f_p = 109$ kHz, while Z_S is capacitive with $f_p = 133$ kHz and $f_{o1}=f_A$. Finally, $L_p = 34.4\ \mu$H and $f_p = 109$ kHz are selected.

B. *Secondary Compensation Design*

With the conventional series compensation of the receivers, cross interference of power channels occurs due to the reduced load quality factor Q_m [15], which can be expressed as

$$Q_m=\frac{\omega_m L_m}{R_{Leqm}}. \tag{20}$$

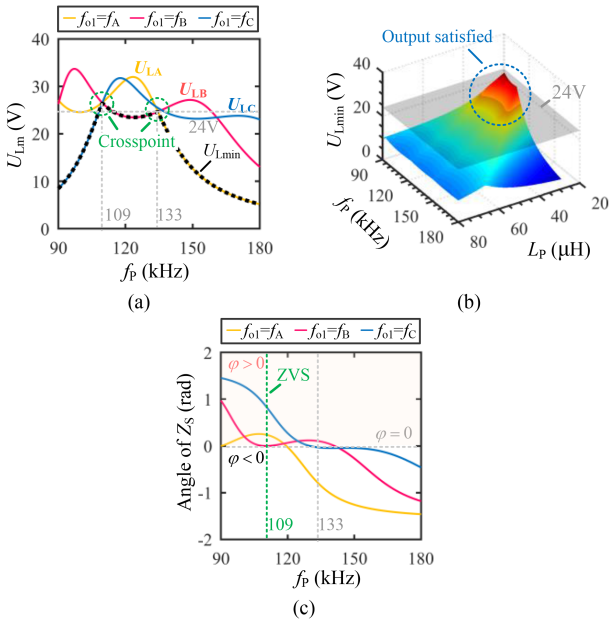

Fig. 5. System performance analysis with different parameters of *LCC* compensation. (a) Relationship between f_P and U_{Lm} in SPEM. (b) Relationship between f_P, L_P, and U_{Lmin}. (c) Relationship between f_P and the input impedance angle φ.

Moreover, it should be noted that the duty cycle of control signals for switches can be regulated to change the motor speed. Hence, odd and even harmonics of operating frequencies coexist in the output of the inverter when the duty cycle is less than 50%. Although a design method of the compensation with parallel *LC* units is proposed to reduce the cross interference from nontargeted resonant frequencies in [15], the interference from the harmonics of the nontargeted resonant frequencies is not considered.

With TFs on the receiving side, there are additional resonant points of the reflected impendence, namely $f_{m\alpha}$ and $f_{m\beta}$, as shown in Fig. 4(c) and (d). Take phase B targeted as an example, when the resonant points $f_{B\alpha}$ and $f_{B\beta}$ are close to the harmonic nf_A ($n = 2, 3\ldots$), the increase of $|Z_{rB}|$ can lead to interference at receiver B. Hence, it is necessary to limit the reflected impedance at the harmonics of nontargeted frequency. The cross interferences from the harmonics can be suppressed by adjusting L_{m1} and L_{m2}.

To quantitatively analyze the relationship between L_{m1}, L_{m2}, and the interference from the harmonics, the multiple harmonics analysis [26] is used in circuit modeling. The output voltage of the dual-frequency-driven inverter is the superposition of two unipolar square waves with different frequencies and the details are discussed in Section IV-A. The unipolar square wave u_{oi} with frequency ω_{oi} can be expressed in the Fourier series and the RMS value of the voltage at frequency $n\omega_{oi}$, namely U_{oi_n}, can be given by

$$U_{oi\_n}=\frac{V_{in}}{n\pi}\sqrt{1-\cos(2\pi n D_{oi})} \tag{21}$$

where D_{oi} is the duty cycle of control signals for bridge leg i in the inverter. The cross-interference should be suppressed when

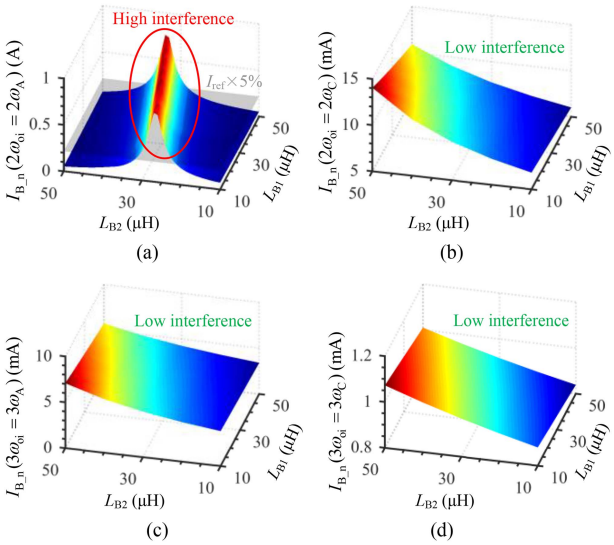

Fig. 6. Relationship between L_{B1}, L_{B2} and the interference in phase B from the harmonics of nontargeted frequencies. (a) Analysis of the interference at $2\omega_A$. (b) Analysis of the interference at $2\omega_C$. (c) Analysis of the interference at $3\omega_A$. (d) Analysis of the interference at $3\omega_C$.

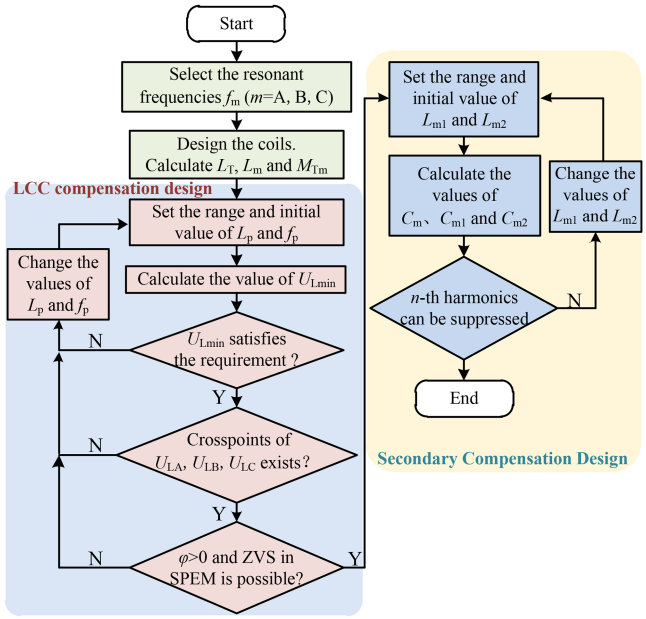

Fig. 7. Design procedure of the proposed decoupled multifrequency MR/MP wireless SRM system.

the harmonic source is maximized. When D_{oi} equals to $1/2n$, U_{oi_n} achieves its maximum value of $1.414V_{in}/\ n\pi$.

With the equivalent ac source of $U_S = 1.414V_{in}/n\pi$, the RMS value of the current of the receiving coils at $n\omega_{oi}$ can be solved with (6) by replacing ω_{oi} in (6) and (7) with $n\omega_{oi}$. Take the design of L_{B1} and L_{B2} as an example, the RMS value of interference currents at the frequency $n\omega_A$ and $n\omega_C$ in phase B, namely I_{B_n} ($n\omega_{oi} = n\omega_A$) and I_{B_n} ($n\omega_{oi} = n\omega_C$), are calculated with variable L_{B1} and L_{B2}, and the interference of second and third harmonics are shown in Fig. 6. The interference currents at the third and higher order harmonics can be virtually filtered out. However, the interference current can reach up to 1 A when $2\omega_{oi} = 2\omega_A$, and it is almost 23% of I_{ref}, which is the required current for receiving coils. Hence, the L_{B1} and L_{B2} should be designed carefully. To minimize the cross-interference, the current at the nontarget resonant frequencies should be limited to 5% of I_{ref}, and the design details are as follows.

At first, the operating frequencies, namely f_A, f_B, and f_C, and the inductance of receiving coils, namely L_A, L_B, and L_C should be determined. Then, the initial range of L_{m1} and L_{m2} is set to 10–50 μH and the corresponding C_{m1}, C_{m2}, and C_m can be decided according to (2)–(5) with the preset f_m. Finally, according to the relationship between L_{m1}, L_{m2}, and the interference from the harmonics, the inductors of the TFs that satisfy (22) are selected

$$\begin{cases} \left|\dot{I}_{A\_n}(n\omega_{oi}=n\omega_B)\right| \le 5\% \times I_{ref} \\ \left|\dot{I}_{A\_n}(n\omega_{oi}=n\omega_C)\right| \le 5\% \times I_{ref} \\ \left|\dot{I}_{B\_n}(n\omega_{oi}=n\omega_A)\right| \le 5\% \times I_{ref} \\ \left|\dot{I}_{B\_n}(n\omega_{oi}=n\omega_C)\right| \le 5\% \times I_{ref} \\ \left|\dot{I}_{C\_n}(n\omega_{oi}=n\omega_A)\right| \le 5\% \times I_{ref} \\ \left|\dot{I}_{C\_n}(n\omega_{oi}=n\omega_B)\right| \le 5\% \times I_{ref} \end{cases} (n=2,3,\ldots). \quad (22)$$

C. Summary of the System Circuit Design Procedure

As aforementioned, the system circuit design procedure is summarized in Fig. 7, and the parameters in Table I are utilized in experiments. First, the operating frequency is selected based on the transmission distance and efficiency. Then, according to the wounded coil inductances, the compensation parameters of the primary side which meets the rated voltage output, power balance, and soft-switching requirements are searched. Finally, the parameters of the TFs and the series capacitances on the secondary side are selected based on the resonant relationship of the receivers, and the cross interference from harmonics of nontargeted frequencies is evaluated.

IV. Control Strategy

A. Dual-State Drive Method of the Inverter

Driving states of the inverter in SPEM and DPEM are shown in Fig. 8. u_{o1} and u_{o2} are the voltage at the midpoint of the bridge legs I and II, respectively. T_{o1} and T_{o2} are the driving signal periods of the switches in the bridge legs I and II, respectively. The basic principle is that the ideal control signals of the two switches in a bridge leg are complementary. Generally, there are two possible driving states in SPEM, namely, the conventional single-frequency FB-driven state and the proposed single-frequency HB-driven state. The former one employed PWM signals at the same frequency to drive the switches in two bridge legs, which means $T_{o1} = T_{o2}$, as shown in Fig. 8(a). However, the latter one makes the FB inverter to work as an HB inverter by cutting off Q_3 and maintaining conduction of Q_4, as shown in Fig. 8(b). Moreover, the dual bridge legs operate at different frequencies in DPEM, which means $T_{o1} \neq T_{o2}$ in this mode, as shown in Fig. 8(c).

In this article, the operating modes are switched to achieve the phase-overlapped excitation of the motors, and the stable voltage outputs are required to reduce the torque ripple. With

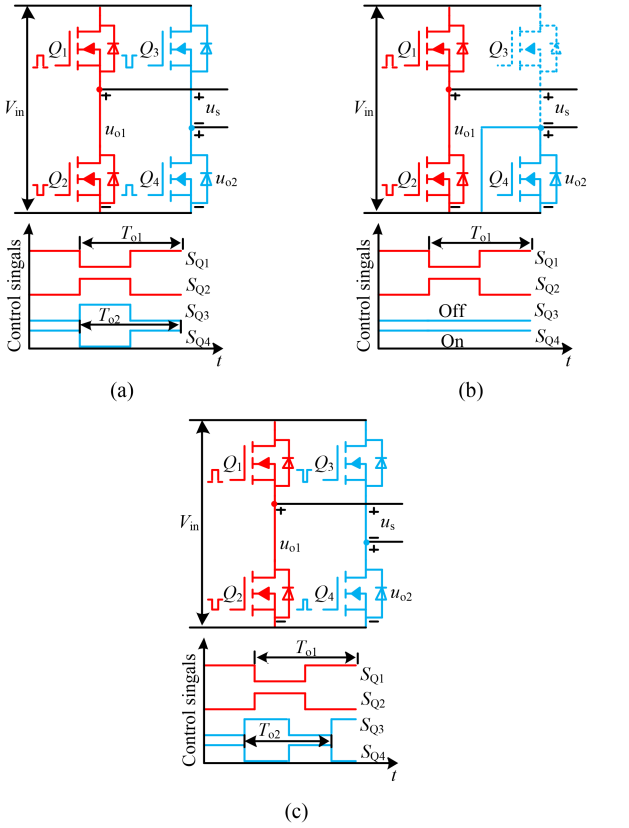

Fig. 8. Driving states of the inverter. (a) Single-frequency FB-driven state in SPEM. (b) Single-frequency HB-driven state in SPEM. (c) Dual-frequency FB-driven state in DPEM.

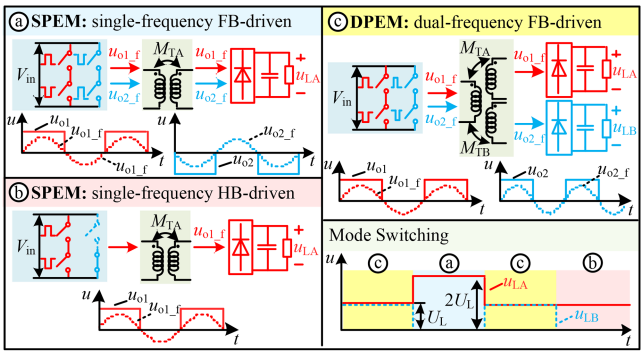

Fig. 9. Comparison of the driving states with open-loop operation.

open-loop operation, the driving states are compared in Fig. 9, where u_{o1_f} and u_{o2_f} are the fundamental components of u_{o1} and u_{o2}, respectively. In the DPEM, each target phase is excited by the single bridge leg and the targeted load voltage is denoted as U_L. In single-frequency FB-driven state, $|u_{o1\_f}|$ is equal to $|u_{o2\_f}|$ and both bridge legs are used to convert power to the target. Hence, the targeted load voltage becomes $2U_L$ in SPEM, and a voltage ripple of the target phase can be generated once mode switch occurs. Instead, only single bridge leg is utilized to energize the target with the proposed single-frequency HB-driven state in SPEM, thus stabilizing the voltage outputs.

In DPEM, when $f_{o1} = f_m$ and $f_{o2} = f_g$, the corresponding excitation phases of bridge legs I and II are phase m and phase g, respectively. In SPEM, the bridge leg I operates at frequency

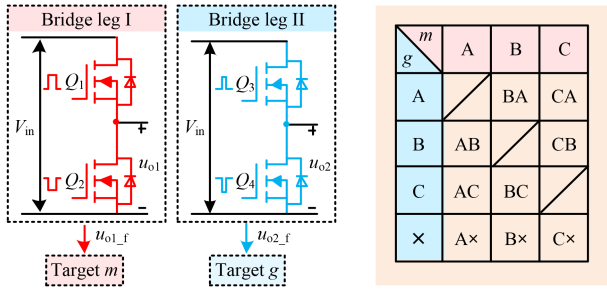

g \ m	A	B	C
A		BA	CA
B	AB		CB
C	AC	BC	
×	A×	B×	C×

Fig. 10. Relationship between bridge legs of the inverter and the corresponding excitation phases.

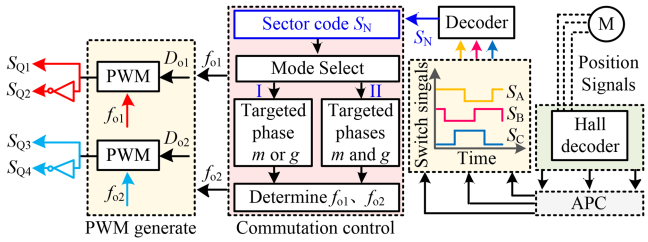

Fig. 11. Hybrid excitation strategy.

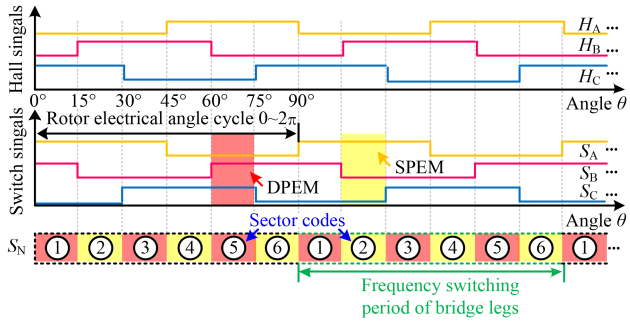

Fig. 12. Selection of sectors in the commutation control sequence.

$f_{o1} = f_m$, and phase m is the corresponding excitation target, while bridge leg II operates at frequency $f_{o2} = 0$ Hz and does not correspond to any excitation phase, denoted as $g = \times$. The relationship between the bridge legs of the inverter and the corresponding excitation phases is shown in Fig. 10.

B. Hybrid Excitation Strategy

The wireless SRM system selects the operating frequency according to the rotor position and excites each phase winding in turn within the phase inductance rise region to obtain a continuous positive torque. Taking a 6/4-pole SRM as an example, conventional systems set the length of conduction interval in APC to be 30° in a rotor angle cycle [10], [11]. Hence, there is no overlap in the conduction interval of the phases and the phase inductance rise interval is not fully utilized by the conventional wireless SRM, resulting in a limited motor torque.

To solve the aforementioned issue, a hybrid excitation strategy is proposed to achieve the overlapped excitation of windings, as shown in Fig. 11, where D_{o1} and D_{o2} are the pulse width of the inverter control signals. At first, the rotor position is first resolved by hall signals and then APC is used to generate the switch signals. Then, S_N, which is the sector number of the

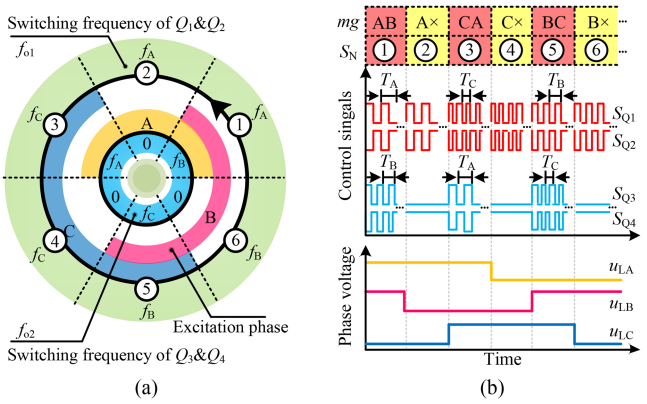

Fig. 13. Operating principles of the commutation control. (a) Commutation control sequence. (b) Operating waves with $D_{o1} = D_{o2} = 50\%$.

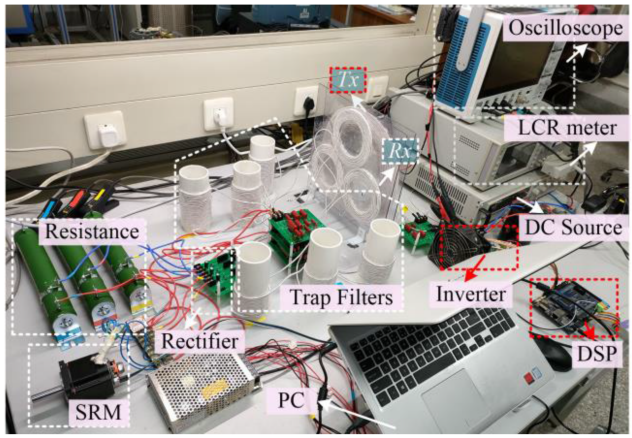

Fig. 14. Experimental setup of the proposed wireless SRM system.

TABLE II
COIL PARAMETERS

Items	Value
Outer diameter of coils (*Tx*/*Rx*)	280/128 mm
Turns of coils (*Tx*/*Rx*)	21/9×3
Air gap between *Tx* and *Rx*	30 mm
Outer diameter of Litz wires	2.5 mm

commutation control sequence, can be obtained by decoding the switch signals, as shown in Fig. 12. Based on the commutation control sequence, the operating mode, targeted excitation phase(s), and the operating frequencies are located in the sector S_N, as shown in Fig. 13. Finally, if DPEM is enabled, phase m and phase g are energized, while phase m can be excited in SPEM.

As depicted in Fig. 12, θ is the rotor angle and a rotor angle cycle is 0°–90° for a 6/4-pole SRM, which can be denoted as electrical angle 0–2π. The switch signals S_A, S_B, and S_C are the excitation signals for phases A, B, and C, respectively. A high level of the switch signal indicates that the corresponding phase is excited, while a low level means that the corresponding phase picks up no energy. Then, S_A, S_B, and S_C can be decoded into S_N by a linear transformation.

TABLE III
COMPARISON OF THE WIRELESS SRMS

Ref.	[24]	[10]	[11]	Proposed
Compensation*	LCC-S	Switched capacitor-S	LCC-S	LCC-TF filter & S
Secondary active parts	Yes	No	No	No
Phase overlapped excitation	No	No	No	Yes
Power equalization	Yes	No	Yes	Yes
Number of switches	7	8	4	4
Number of frequencies	1	3	3	3
Receiving coil (Size/mm)+	Circular (260)	Rectangular (300×200)	Rectangular (210×150)	Circular (128)
Minimum load quality factor	2.88	27	10.27	2.19
WPT efficiency	96%	72.8%	80%	82.3%

* *LCC*: inductor-capacitor-inductor; S: series; Trap filter & S: dual *LC* filters in series with a capacitor.
+ Circular coil: outer diameter; Rectangular coil: length×width; Units: mm.

The commutation order of the windings is set offline according to the direction of rotation, and the preset order here is AB-A-CA-C-BC-B-AB. Then, in a 6/4 pole SRM, take the turn-on angle $\theta_{on} = 0°$ and turn-off angle $\theta_{off} = 45°$ in APC as an example, the commutation control sequence can be obtained as shown in Fig. 13(a). This sequence contains a frequency switching period of bridge legs, which has the same length as a rotor angle cycle. The period is divided into six sectors according to excitation targets. The operating frequencies f_{o1} and f_{o2} as well as the excitation targets m and g can be located in the sequence according to the sector number S_N. Take $S_N = 1$ as an example, the operating mode is selected to be DPEM, and phase A as well as phase B are the target excitation phases. Hence, f_{o1} and f_{o2} are set to f_A and f_B, respectively. With the commutation control, the operating waves with $D_{o1} = D_{o2} = 50\%$, are shown in Fig. 13(b), where $T_m = 1/f_m$.

V. EXPERIMENT RESULTS

As shown in Fig. 14, an experimental prototype is built to validate the effectiveness of the proposed wireless SRM system and its control methods. The dc power supply IT6516C is used as the voltage source. In the transmitter, the MOSFET SPW47N60C3 is adopted as the switch for the inverter, with its control signal provided by DSP28335. The single-layer transmitting coils (*Tx*) and triple-layer receiving coils (*Rx*) are wound with 0.1mm×300 strands of Litz wire. The parameters shown in Tables I and II are measured by LCR meter.

The experiment is divided into two steps. First, a steady-state analysis is conducted based on a 5.2 Ω resistive load to demonstrate the cross-interference resistance of the TFs and the effectiveness of the dual-state drive method. Second, a 6/4-pole SRM is used as the load to further verify the power balance of each phase of the motor and analyze performance indicators,

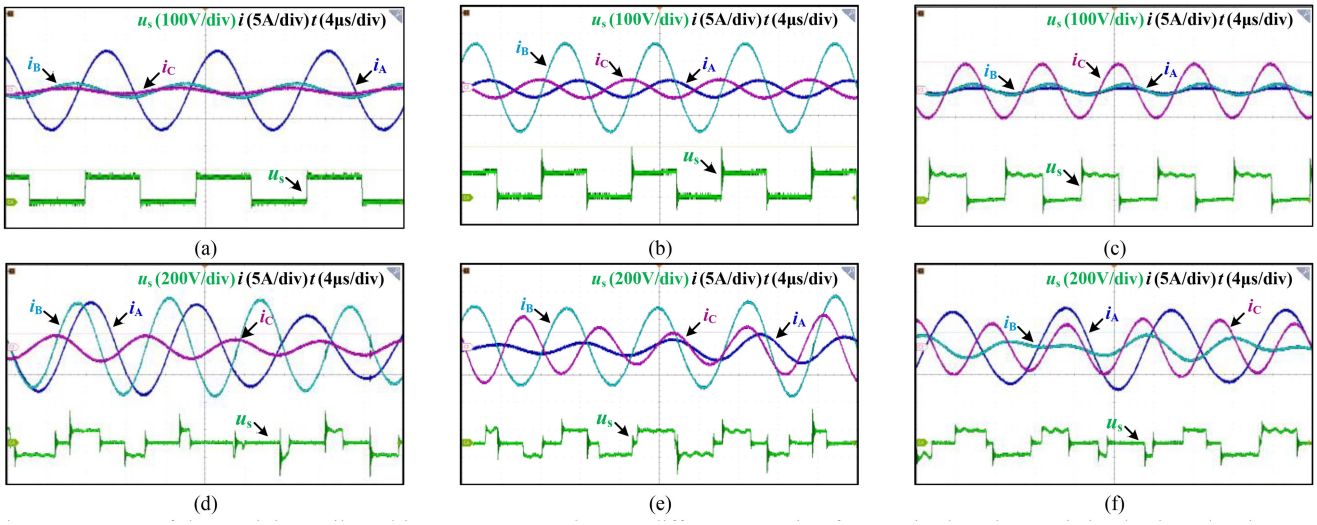

Fig. 15. Current of the receiving coils and inverter output voltage at different operating frequencies based on resistive loads and series compensation in the receiving side. (a) $f_{o1} = f_A = 90$ kHz and $f_{o2} = 0$ Hz. (b) $f_{o1} = f_B = 110$ kHz and $f_{o2} = 0$ Hz. (c) $f_{o1} = f_C = 130$ kHz and $f_{o2} = 0$ Hz. (d) $f_{o1} = f_A = 90$ kHz and $f_{o2} = f_B = 110$ kHz. (e) $f_{o1} = f_B = 110$ kHz and $f_{o2} = f_C = 130$ kHz. (f) $f_{o1} = f_C = 130$ kHz and $f_{o2} = f_A = 90$ kHz.

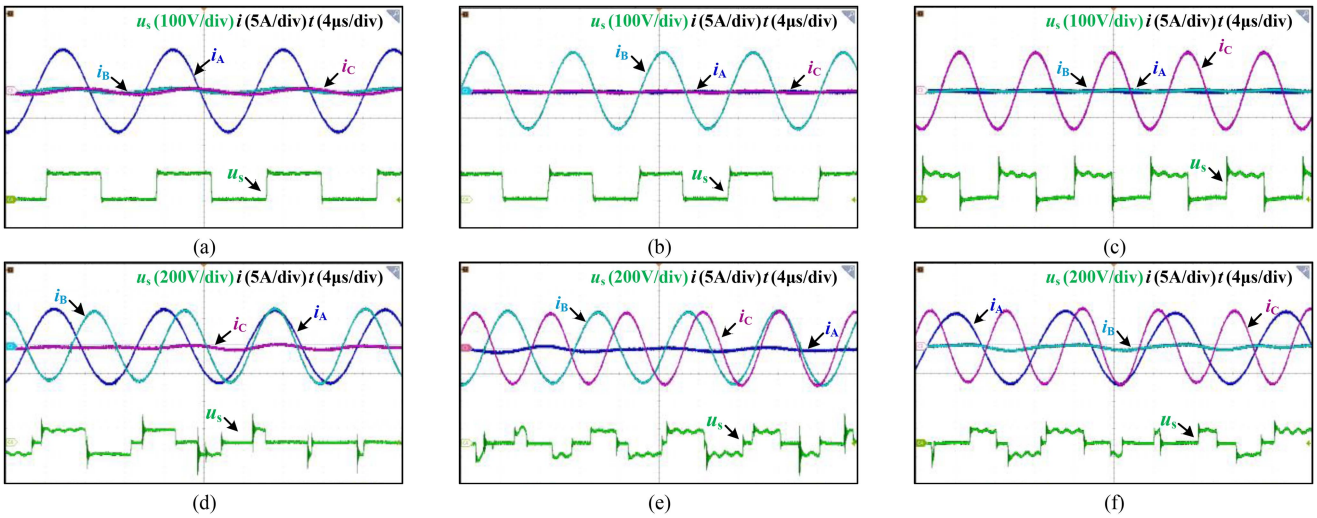

Fig. 16. Current of the receiving coils and inverter output voltage at different operating frequencies based on resistive loads and the proposed TFs. (a) $f_{o1} = f_A = 90$ kHz and $f_{o2} = 0$ Hz. (b) $f_{o1} = f_B = 110$ kHz and $f_{o2} = 0$ Hz. (c) $f_{o1} = f_C = 130$ kHz and $f_{o2} = 0$ Hz. (d) $f_{o1} = f_A = 90$ kHz and $f_{o2} = f_B = 110$ kHz. (e) $f_{o1} = f_B = 110$ kHz and $f_{o2} = f_C = 130$ kHz. (f) $f_{o1} = f_C = 130$ kHz and $f_{o2} = f_A = 90$ kHz.

including speed and efficiency. It should be noted that each winding is in series with a resistor of 4 Ω and the equivalent internal winding resistance is 5 Ω.

The traditional wireless SRM employs series compensation on the receiving side. However, cross-interference may occur when the load quality factor is reduced. Based on resistive loads and series compensation on the receiving side, the current in the receiving coils at different operating frequencies is shown in Fig. 15. It can be seen that there is significant cross-interference between each channel. In SPEM, $f_{o1} = f_B = 110$ kHz and $f_{o2} = 0$ Hz are analyzed as an example. Although phase B can be excited at a working frequency of f_B, serious interference is generated for the nontarget phases, namely phases A and C. The current in the nontarget phases, i_A and i_C, is approximately 20% of the current i_B in the target phase. This is because the magnitudes of $|Z_{rA}|$ and $|Z_{rC}|$ are significant compared to $|Z_{rB}|$ at 110 kHz, as shown in Fig. 4(a). In DPEM, although it is possible to excite two target phases using a dual-state drive method, cross-interference results in distorted current in the target phase and unintentional excitation of the nontarget phases.

To address the aforementioned issues, TFs are utilized to suppress cross interference. In Fig. 16, the current of the receiving coils in the nontarget phases is within 5% of that in the target phases, demonstrating the effectiveness of TFs. Moreover, thanks to the dual-state drive method and the design of the *LCC* network, the rms value of the coil current in the target phases is almost the same as 5.3 A, as shown in Fig. 16, and the load current of the target phases are almost the same as 4.8 A, as shown in Fig. 17. Hence, balanced excitation of each phase can be achieved under time-division multiplexing conditions.

Furthermore, as shown in Fig. 17(a), (b), and (c), the output current of the inverter lags behind the output voltage in SPEM.

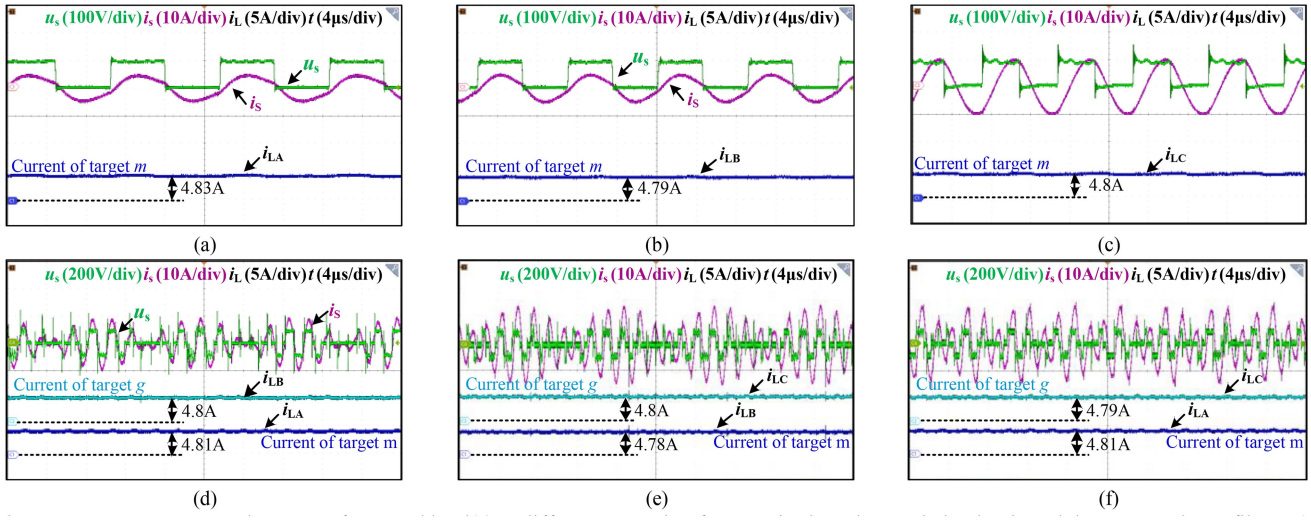

Fig. 17. Inverter outputs and current of targeted load(s) at different operating frequencies based on resistive loads and the proposed TFs. (a) $f_{o1} = f_A = 90$ kHz and $f_{o2} = 0$ Hz. (b) $f_{o1} = f_B = 110$ kHz and $f_{o2} = 0$ Hz. (c) $f_{o1} = f_C = 130$ kHz and $f_{o2} = 0$ Hz. (d) $f_{o1} = f_A = 90$ kHz and $f_{o2} = f_B = 110$ kHz. (e) $f_{o1} = f_B = 110$ kHz and $f_{o2} = f_C = 130$ kHz. (f) $f_{o1} = f_C = 130$ kHz and $f_{o2} = f_A = 90$ kHz.

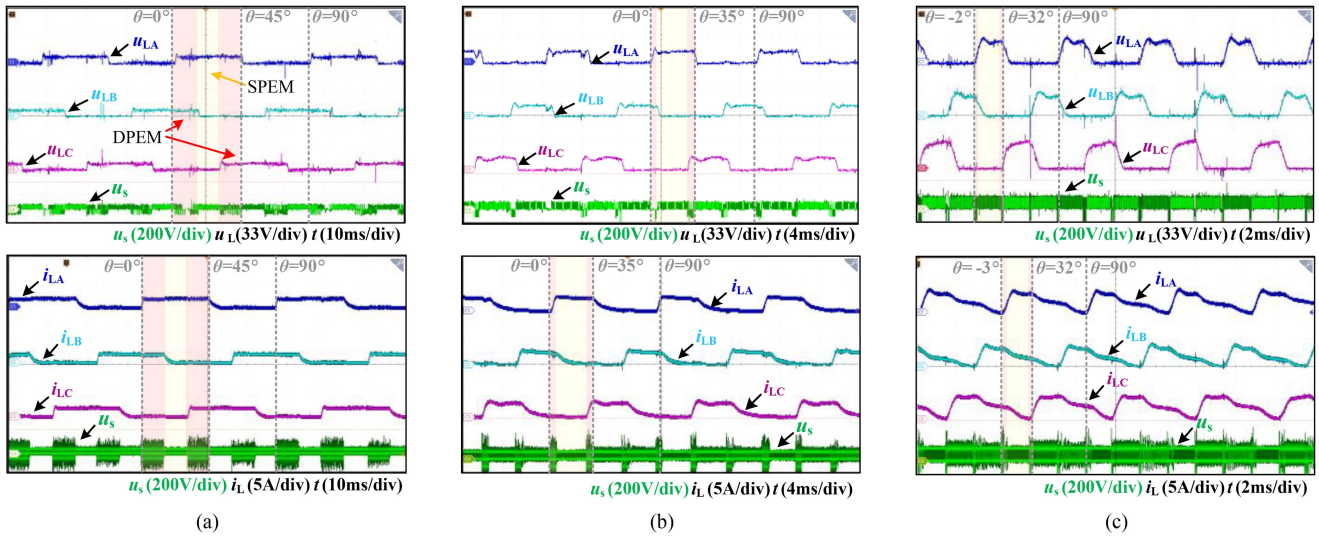

Fig. 18. Output voltage and current of the motor-load system with variable dc source V_{in} based on hybrid excitation strategy. (a) $V_{in} = 36$ V and $\omega_{SRM} = 450$ r/min. (b) $V_{in} = 56$ V and $\omega_{SRM} = 1480$ r/min. (c) $V_{in} = 96$ V and $\omega_{SRM} = 3750$ r/min.

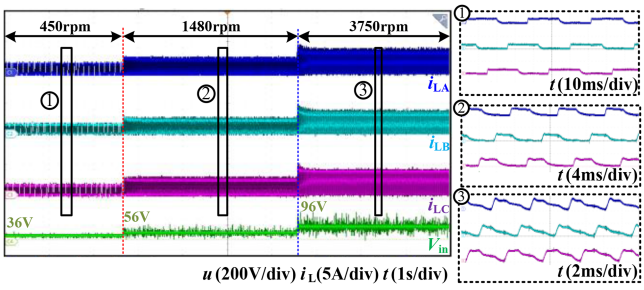

Fig. 19. Transient output current with variable V_{in} based on hybrid excitation strategy.

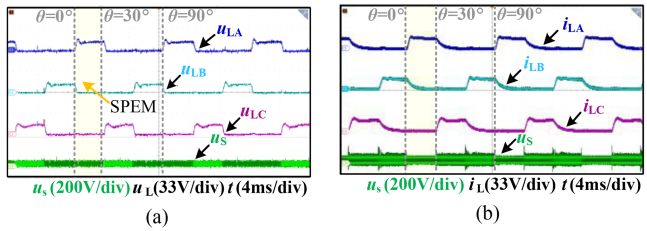

Fig. 20. Outputs of the motor-load system with the conventional nonoverlapped excitation strategy. (a) Output voltage. (b) Output current.

This indicates that the input impedance is inductive. Hence, the current is allowed to flow through the body diode during the power switch turn-on process, and achieve zero-voltage turn-on when the duty cycle of the control signals is 50%. Additionally, the current during the switch transition is only around 1 A when the operating frequency is 90 and 110 kHz, further reducing the losses of the inverter. However, when the operating frequency is 130 kHz, the imaginary part of the input impedance is large.

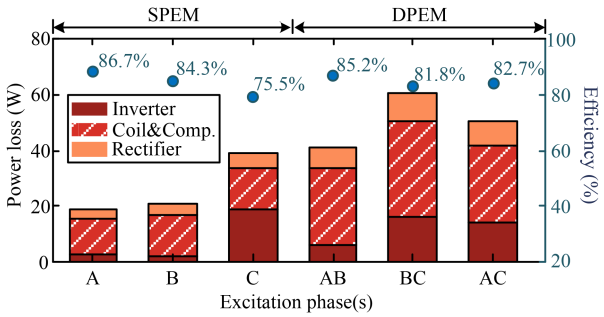

Fig. 21. Transmission efficiency and power loss of the proposed wireless SRM.

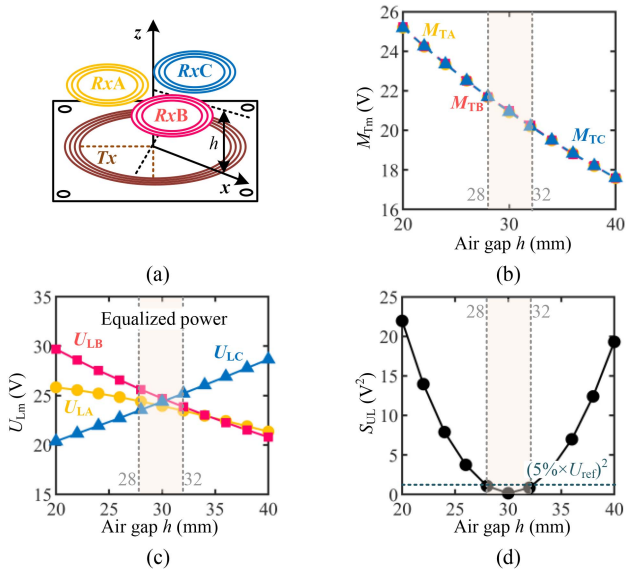

Fig. 22. System performance analysis with variations of distance h when $d = 0$ mm. (a) Coil position. (b) Relationship between h and the mutual inductance M_{Tm}. (c) Relationship between h and U_{Lm}. (d) Relationship between h and S_{UL}.

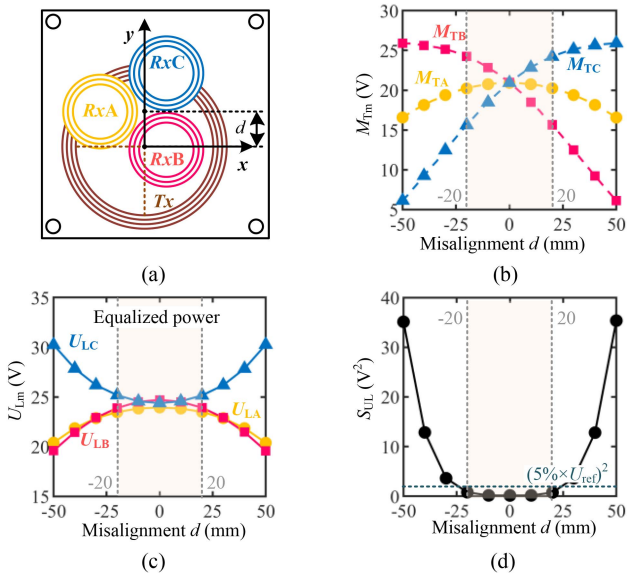

Fig. 23. System performance analysis with variations of horizontal misalignment d when $h = 30$ mm. (a) Coil position. (b) Relationship between d and the mutual inductance M_{Tm}. (c) Relationship between d and U_{Lm}. (d) Relationship between d and S_{UL}.

As a result, there is a large phase lag of the current, and i_s is approximately 9.4 A during the switch transition, causing significant switch-off losses of the inverter.

To verify the effectiveness of the hybrid excitation strategy, the experiment is conducted with a 6/4-pole SRM load. The conventional wireless SRM energizes the phase windings one by one, resulting in restricted torque output. To solve this issue, the hybrid excitation strategy is utilized to achieve the overlapped control. To attain better performance of the motor, the turn-on angle θ_{on} and turn-off angle θ_{off} in APC are set based on the motor speed ω_{SRM} as follows.

1) $\omega_{\mathrm{SRM}}<500$: Parameters of APC are $\theta_{\mathrm{on}} = 0°$ and $\theta_{\mathrm{off}} = 45°$. In this case, the motor is in a self-starting state and the rising zone of the winding inductance is fully utilized to achieve the maximum motor torque.
2) $500\leq\omega_{\mathrm{SRM}}<2000$: Parameters of APC are $\theta_{\mathrm{on}} = 0°$ and $\theta_{\mathrm{off}} = 35°$. By turning off the excitation of the windings in advance, the free-wheeling current in the declining zone of the winding inductance is reduced.
3) $\omega_{\mathrm{SRM}}\geq2000$: Parameters of APC are $\theta_{\mathrm{on}} = -3°$ and $\theta_{\mathrm{off}} = 32°$. By turning on the excitation in advance, a larger current is established in the flat zone of the winding inductance.

According to the above rules, the outputs with variable dc sources are measured when the motor runs with no load. The steady-state outputs at dc voltages of 36, 56, and 96 V are shown in the Fig. 18, while the transient waveforms are shown in the Fig. 19.

With a dc power supply voltage of 56 V, the hybrid excitation strategy is compared with the conventional nonoverlapped excitation strategy, as shown in Figs. 18(b) and 20. It can be observed that the power of each phase winding is balanced, and there is minimal cross-interference. With the nonoverlapped excitation strategy, $\theta_{\mathrm{on}} = 0°$ and $\theta_{\mathrm{off}} = 30°$ and the no-load speed of the motor is almost 1250 r/min, which is 230 r/min lower than the speed with hybrid excitation. The above characteristics successfully demonstrate the effectiveness of the hybrid excitation strategy.

With rated power operation, the power losses and transmission efficiency in different operating modes are analyzed in Fig. 21. In SPEM, when phase A and phase B are excited separately, ZVS effectively reduces the switching losses of the inverter, and the losses of the coil and compensation circuit dominate the transmission efficiency. When phase C is driven, the efficiency decreases due to the larger turn-off losses. In addition, the losses of the rectifier increase with the frequency. Moreover, the dual-phase excitation efficiency is between the efficiencies of the single-phase excitation for each target phase. When $\theta_{\mathrm{on}} = 0°$ and $\theta_{\mathrm{off}} = 35°$, the average transmission efficiency is almost 82.3%, which is higher than that of the traditional multifrequency wireless SRM [10], [11].

VI. Discussion

A conventional SRM system relies on cables to transmit power and drive the motor. However, in the hyperthermia and humidity working conditions, or cross-media power supply situations, wire harness connections reduce the reliability and flexibility of the drive module. Wireless SRM is a viable solution and there are two implementations: 1) the first one uses WPT for isolated

energy supply, while the secondary active converter is used to control the motor speed and torque; 2) the second one not only offers isolated power for the motor but also integrates motor control into the transmitter, thus entirely removing the motor-side controller and its associated auxiliary power supply. The comparison of wireless SRMs is shown in Table III. Although the first type of wireless SRM has higher WPT efficiency, this system requires approximately twice the number of switches as the proposed one, and the active converter on the motor side is prone to frequent failures [24]. Literature works [10] and [11] adopt the multifrequency multireceiver structure to implement the second type of wireless SRM. This structure avoids the risk of motor-side active switch failure due to harsh environments, thus improving system reliability and reducing maintenance costs. Compared with traditional multifrequency wireless SRM [10], [11], the proposed system has the following advantages:

1) phase-overlapped excitation;
2) stable operation under reduced load power factor;
3) higher transmission efficiency.

Potential applications include sewage pumps and robots in underground pipes.

The transmission distance h and misalignment d may vary in practical applications, which can degrade system performance. Figs. 22 and 23 illustrate the system performance with coupling variations. The variance of U_{LA}, U_{LB}, and U_{LC} is denoted as S_{UL}. If S_{UL} satisfies (23), the power of the phase windings is considered balanced. It can be observed that the system maintains power balance within a tolerance range of 28–32 mm for distance, as shown in Fig. 22, and a range of −20 to 20 mm for horizontal misalignment, as shown in Fig. 23. Additionally, a large offset can result in a power imbalance. Therefore, the proposed system should be avoided in situations involving significant misalignment and distance variations

$$S_{\mathrm{UL}} \leq (5\% \times U_{\mathrm{ref}})^2. \tag{23}$$

In the proposed system, the power losses of the inverter, coils, and compensating networks account for a large proportion of system losses. The *LCC* compensation in the transmitter has only one optimal resonant frequency, which is different from the resonant frequencies of the receivers. The target receiver can be fully resonant, but the nonresonance state at the transmitter may result in a large input impedance angle, thereby increasing the switch-off losses of the inverter, as shown in Fig. 17(c), (e), and (f). Therefore, the passive multifrequency resonant tank of the transmitter should be a direction in the future. Additionally, the loss of the magnetic coupler can be minimized by optimizing the coil size and structure. Furthermore, the inductors in the TFs can be reduced in size and improve transmission efficiency by winding orthogonally or configuring ferrite cores.

VII. Conclusion

In this article, a novel decoupled multifrequency wireless SRM system with a hybrid excitation strategy is proposed to ensure reliable phase-overlapped excitation for SRM. The key features of the work are as follows.

1) By optimizing the *LCC* compensation network, the system power balance was achieved. The ZVS operation control of the inverter was achieved during SPEM, which improves the system efficiency.
2) TFs are optimized and implemented to minimize cross-interference from nontargeted frequencies. The optimal circuit modeling and overall design procedure of the proposed wireless SRM are developed.
3) With the dual-state drive method, the selection of single or dual excitation phases is allowed and target phase voltage ripple during mode switch can be reduced.
4) By employing a hybrid excitation strategy, the commutation of the SRM is achieved and variable turn-on and turn-off angle control is utilized for better motor performance.

The proposed system requires no active switches or controllers in the motor side, which is desirable to apply to harsh environments. Compared with conventional wireless SRM, the proposed system realizes larger torque output and higher transmission efficiency.

References

[1] B. Zhang et al., "Triple-coil-structure-based coil positioning system for wireless EV charger," *IEEE Trans. Power Electron.*, vol. 36, no. 12, pp. 13515–13525, Dec. 2021.
[2] H. Sekiya, K. Tokano, W. Zhu, Y. Komiyama, and K. Nguyen, "Design procedure of load-independent class-e WPT systems and its application in robot arm," *IEEE Trans. Ind. Electron.*, vol. 70, no. 10, pp. 10014–10023, Oct. 2023.
[3] H. Zhuang, W. Wang, K. Zhao, S. Kuang, Z. Wang, and G. Yan, "Efficient power receiving coil with novel ferrite core structure for capsule robot," *IEEE Trans. Biomed. Circuits Syst.*, vol. 16, no. 5, pp. 939–946, Oct. 2022.
[4] H. Yin, M. Fu, M. Liu, J. Song, and C. Ma, "Autonomous power control in a reconfigurable 6.78-MHZ multiple-receiver wireless charging system," *IEEE Trans. Ind. Electron.*, vol. 65, no. 8, pp. 6177–6187, Aug. 2018.
[5] M. Ishihara, K. Fujiki, K. Umetani, and E. Hiraki, "Autonomous system concept of multiple-receiver inductive coupling wireless power transfer for output power stabilization against cross-interference among receivers and resonance frequency tolerance," *IEEE Trans. Ind. Appl.*, vol. 57, no. 4, pp. 3898–3910, Jul./Aug. 2021.
[6] Z. Pantic, K. Lee, and S. M. Lukic, "Receivers for multifrequency wireless power transfer: Design for minimum interference," *IEEE J. Emerg. Sel. Topics Power Electron.*, vol. 3, no. 1, pp. 234–241, Mar. 2015.
[7] C. Qi, S. Huang, X. Chen, and P. Wang, "Multifrequency modulation to achieve an individual and continuous power distribution for simultaneous MR-WPT system with an inverter," *IEEE Trans. Power Electron.*, vol. 36, no. 11, pp. 12440–12455, Nov. 2021.
[8] W. Han, K. T. Chau, Z. Hua, and H. Pang, "Compact wireless motor drive using orthogonal bipolar coils for coordinated operation of robotic arms," *IEEE Trans. Magn.*, vol. 58, no. 2, Feb. 2022, Art. no. 8200608.
[9] L. Fang et al., "Design of wireless individual-drive system for variable-reluctance stepping motor," *IEEE Trans. Circuits Syst. II-Exp. Briefs*, vol. 69, no. 4, pp. 2141–2145, Apr. 2022.
[10] C. Jiang, K. T. Chau, C. Liu, and W. Han, "Design and analysis of wireless switched reluctance motor drives," *IEEE Trans. Ind. Electron.*, vol. 66, no. 1, pp. 245–254, Jan. 2019.
[11] C. Jiang, K. T. Chau, W. Liu, C. Liu, W. Han, and W. H. Lam, "An LCC-compensated multiple-frequency wireless motor system," *IEEE Trans. Ind. Informat.*, vol. 15, no. 11, pp. 6023–6034, Nov. 2019.
[12] W. Han, K. T. Chau, Z. Hua, and H. Pang, "An integrated wireless motor system using laminated magnetic coupler and commutative-resonant control," *IEEE Trans. Ind. Electron.*, vol. 69, no. 5, pp. 4342–4352, May 2022.
[13] Y. Chen, C. Gan, H. Shi, K. Ni, and R. Qu, "Active power allocation strategy for a novel wireless open-winding motor system with improved antimisalignment capability," *IEEE Trans. Ind. Electron.*, vol. 70, no. 12, pp. 12071–12081, Dec. 2023.
[14] N. R, "Cross interference free dual frequency wireless power transfer using frequency bifurcation for dynamic biomedical implants," *IEEE Trans. Electromagn. Compat.*, vol. 63, no. 1, pp. 286–293, Feb. 2021.
[15] F. Liu, Y. Yang, Z. Ding, X. Chen, and R. M. Kennel, "Eliminating cross interference between multiple receivers to achieve targeted power distribution for a multi-frequency multi-load MCR WPT system," *Int. Eng. Technol. Power Electron.*, vol. 11, no. 8, pp. 1321–1328, Feb. 2018.

[16] K. Li, W. Ding, J. Yuan, and C. Du, "A decoupled multichannel based wireless SRM system with tunable compensation network and multifrequency pulse density control," *IEEE Trans. Ind. Electron.*, vol. 71, no. 2, pp. 1468–1480, Feb. 2024.
[17] F. Liu, Y. Yang, Z. Ding, X. Chen, and R. M. Kennel, "A multifrequency superposition methodology to achieve high efficiency and targeted power distribution for a multiload MCR WPT system," *IEEE Trans. Power Electron.*, vol. 33, no. 10, pp. 9005–9016, Oct. 2018.
[18] W. Liu, K. T. Chau, C. H. T. Lee, C. Jiang, W. Han, and W. H. Lam, "Multi-frequency multi-power one-to-many wireless power transfer system," *IEEE Trans. Magn.*, vol. 55, no. 7, Jul. 2019, Art. no. 8001609.
[19] Y. Liu, C. Liu, X. Gao, and S. Liu, "Design and control of a decoupled multichannel wireless power transfer system based on multilevel inverters," *IEEE Trans. Power Electron.*, vol. 37, no. 8, pp. 10045–10060, Aug. 2022.
[20] D. Thenathayalan and J.-H. Park, "Individually regulated multiple-output WPT system with a single PWM and single transformer," *IEEE J. Emerg. Sel. Topics Power Electron.*, vol. 8, no. 4, pp. 3542–3557, Dec. 2020.
[21] C. Xia, N. Wei, H. Zhang, S. Zhao, Z. Li, and Z. Liao, "Multifrequency and multiload MCR-WPT system using hybrid modulation waves SPWM control method," *IEEE Trans. Power Electron.*, vol. 36, no. 11, pp. 12400–12412, Nov. 2021.
[22] A. Walz-Lange and G. Schullerus, "Sensorless control of a switched reluctance machine based on switching frequency evaluation," *IEEE Trans. Ind. Appl.*, vol. 58, no. 4, pp. 4768–4777, Jul./Aug. 2022.
[23] M. A. Gaafar, A. Abdelmaksoud, M. Orabi, H. Chen, and M. Dardeer, "Switched reluctance motor converters for electric vehicles applications: Comparative review," *IEEE Trans. Transp. Electrific.*, vol. 9, no. 3, pp. 3526–3544, Sep. 2023.
[24] W. Ding, K. Li, J. Yuan, J. Li, and C. Du, "Wireless power transmission-based in-wheel switched reluctance motor drive system with an X-type converter," *IEEE Trans. Energy Convers.*, vol. 38, no. 1, pp. 450–462, Mar. 2023.
[25] Z. Zhang, X. Li, H. Pang, H. Komurcugil, Z. Liang, and R. Kennel, "Multiple-frequency resonating compensation for multichannel transmission of wireless power transfer," *IEEE Trans. Power Electron.*, vol. 36, no. 5, pp. 5169–5180, May 2021.
[26] Y. Fang and B. M. H. Pong, "Multiple harmonics analysis for variable frequency asymmetrical pulsewidth-modulated wireless power transfer systems," *IEEE Trans. Ind. Electron.*, vol. 66, no. 5, pp. 4023–4030, May 2019.

Jun Cai (Senior Member, IEEE) received the Ph.D. degree in electrical engineering from the Nanjing University of Aeronautics and Astronautics, Nanjing, China, in 2012.

From 2013 to 2015, he was a EPSRC Research Associate with the Department of Automatic Control and Systems Engineering, University of Sheffield, U.K. Since 2015, he has been a Professor with the Nanjing University of Information Science and Technology (NUIST), Nanjing, China. He is the Deputy Director of Jiangsu Engineering Research Center on Meteorological Energy Using and Control and the director with the NUIST Novel Motor Drive and Control Lab. He is also the Academic Dean and Professor with the School of Mechanical and Electrical Engineering, Anhui Jianzhu University, Hefei, China. He has authored or co-authored over 100 journal and conference papers. He holds 120 patents. His research interests include sensorless technologies, SR/PMSM drives, EV power drive systems, wireless power transfer, and power electronics in renewable energy systems.

Dr. Cai is the Fellow of the royal society for the encouragement of arts, manufactures and commerce (RSA Fellow) and Senior Member of CES.

Bin Li received the B.Eng. degree in electrical engineering from the School of Automation, Nanjing University of Information Science and Technology, China, in 2021. He is currently working toward the M.Sc. degree in electronic information with the Nanjing University of Information Science and Technology, China.

His research interests include wireless power transfer and SR motor drives.

Adrian David Cheok (Senior Member, IEEE) received the Ph.D. degree in electrical engineering from the University of Adelaide, Adelaide, Australia, in 1998.

He is currently a Full Professor with Nanjing University of Information Science and Technology, Director of the Imagineering Institute, Visiting Professor with Raffles University, Malaysia, Visiting Professor with University of Novi Sad-Serbia, on Technical faculty "Mihailo Pupin," Serbia, Faculty with Ducere Business School, and CEO with Nikola Tesla Technologies Corporation. He is a Founder and Director with the Mixed Reality Lab, Singapore. He was formerly Professor with Pervasive Computing, University of London, Full Professor and Executive Dean with Keio University, Graduate School of Media Design and Associate Professor with the National University of Singapore. His research interests include augmented and mixed reality, pervasive and ubiquitous computing, and power electronics.

Dr. Cheok was the recvipient of Australia's highest honor the Order of Australia for his contribution to international education and research by the Governor General of Australia, Representative of Her Majesty the Queen Elizabeth II..

Ying Yan (Member, IEEE) received the Ph.D. degree in electrical and computer engineering from the University of Connecticut, Storrs, CT, US, in 2018.

He is currently a Lecturer with the School of Automation, Nanjing University of Information Science & Technology, Nanjing, China. His research interests include fault detection, diagnosis and prognosis, and machine learning.

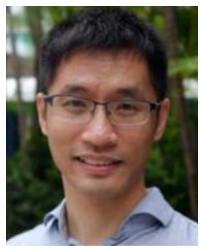

Xin Zhang (Senior Member, IEEE) received the Ph.D. degree in automatic control and systems engineering from the University of Sheffield, Sheffield, U.K., in 2016, and the Ph.D. degree in electronic and electrical engineering from the Nanjing University of Aeronautics and Astronautics, Nanjing, China, in 2014.

From 2014 to 2016, he was a Research Associate with the University of Sheffield. From January to September 2017, he was a Research Fellow with the City University of Hong Kong, Hong Kong. From 2017 to 2020, he was an Assistant Professor with Nanyang Technological University. He is currently a Professor with Zhejiang University, Hangzhou, China. His research interests include power electronics and advanced control theory.

He is the Associated Editor of IEEE Transactions on Industrial Electronics. He has authored and coauthored more than 100 SCI journal papers.